Electronic Supplementary Material (ESI) for Journal of Materials Chemistry A.
This journal is © The Royal Society of Chemistry 2020

Supporting Information

Optical in-situ monitoring during the synthesis of halide perovskite solar cells reveals formation kinetics and evolution of optoelectronic properties

Klara Suchan[a,b], Justus Just[a,c], Pascal Becker[a], Eva L. Unger[b,d] and Thomas Unold*[a]

[a] *Helmholtz-Zentrum Berlin für Materialien und Energie GmbH, Structure and Dynamics of Energy Materials, Hahn-Meitner-Platz 1, 14109 Berlin, Germany*

[b] *Chemical Physics and Nano Lund, Lund University, Box 124, SE-22100, Lund, Sweden Lund, Sweden*

[c] *MAX IV Laboratory, Lund University, PO Box 118, SE-22100 Lund, Sweden*

[d] *Helmholtz-Zentrum Berlin für Materialien und Energie GmbH, Young Investigator Group Hybrid Materials Formation and Scaling, Kekuléstraße 5, 12489 Berlin, Germany*

SI Note 1: XRD analysis of powder samples

For the thin film sample that has not undergone annealing, peaks corresponding to the (001) and (002) diffraction of $MAPbCl_3$ are observed as was shown in Figure 2 of the article. This led to the assumption that $MAPbCl_3$ is a precursor for the $PbCl_2$ derived $MAPbI_3$, while a textured film growth would explain the missing diffraction peaks.

Thus, a powder sample of the not annealed sample was prepared by scratching the thin film off the substrate. In contrast to thin-film samples, powder samples have the advantage, that the crystallites are oriented randomly and thus all reflexes of the crystal structure are visible. Four consecutive scans were performed with each scan taking 6 hours. The fabrication, handling and measurement was always done in nitrogen atmosphere.

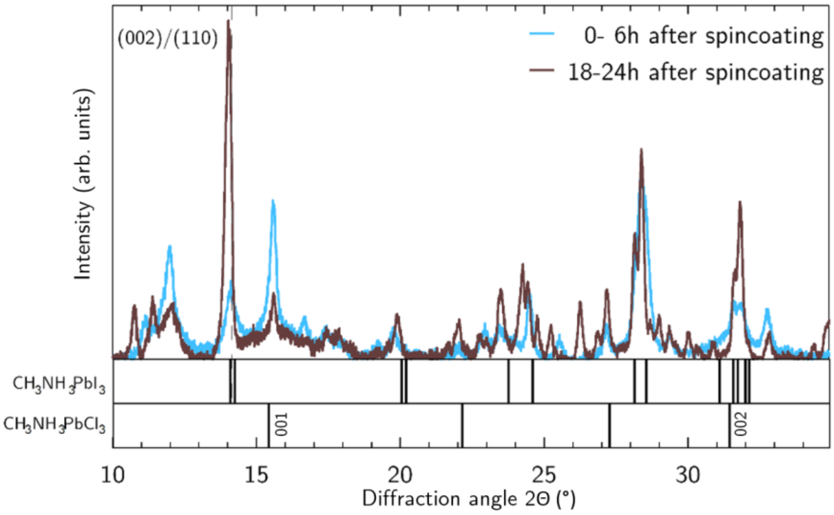

Fig. S1: Powder diffraction pattern of a non-annealed film, taken within the first 6h after spin coating and between 18h and 24h after continuous x-ray exposition in N_2

From the comparison between the powder diffraction pattern and the theoretically expected pattern for $MAPbCl_3$, it becomes clear that, while a multitude of diffraction peaks are visible, the (001) and (002) peaks are over-proportionally large. In a powder sample, this cannot be explained by texturing effects. Rather this suggests that the crystallites are predominantly in a structure similar to 1-dimensional $MAPbCl_3$.[1] Furthermore comparing the consecutive scans, degradation of the sample was observed. During this degradation the 3D diffraction peaks (such as the (111) diffraction peak) rise, indicating that in the course of the degradation three dimensional $MAPbCl_3$ is formed.

Fig. S2 shows the unit cell volume for $MAPbI_{3-x}Cl_x$ samples, as obtained from Rietveld analysis, at various annealing times. It can be seen that the volume of the unit cell of the $MAPbI_{3-x}Cl_x$ phase is below that of pure $MAPbI_3$ for short annealing times but approaches that of pure $MAPbI_3$ for fully annealed films, indicating a decrease of the chlorine content.[1,2] Furthermore a rough estimation of the domain size by the Scherrer equation[3] shows no significant change during annealing.

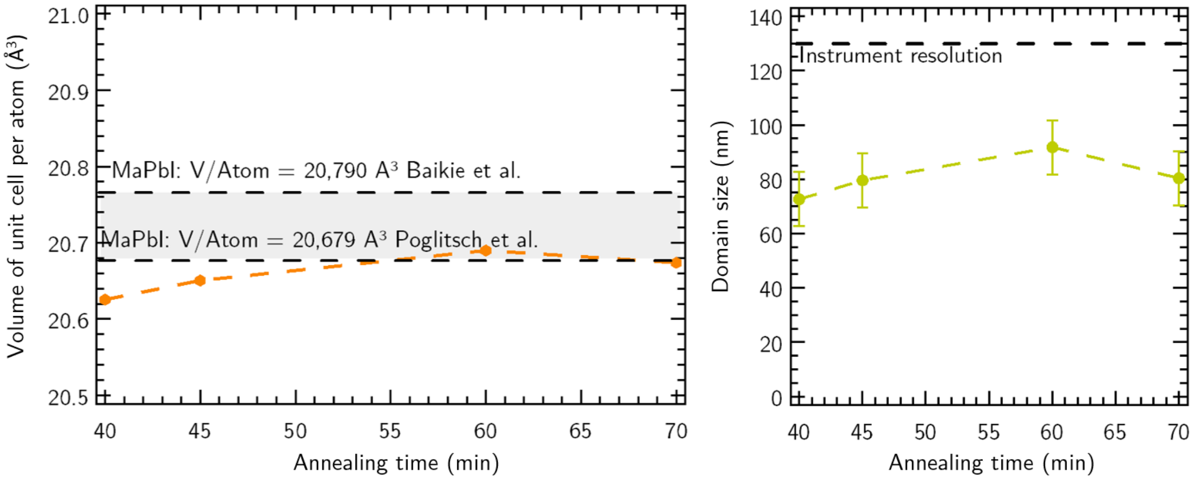

Fig. S2: Volume of the unit cell as obtained from Rietveld analysis for different annealing times. For a comparison literature values of the pure $MAPbI_3$ phase are indicated by dashed lines.

SI Note 2: Fitting of the reflection spectra

In order to fit the reflection spectra it is assumed that the total thickness of the film is constant during the process and that the $MAPbI_3$ phase is distributed homogeneously within the film. The film thickness of 300 nm has been measured using a SEM cross section as shown for a typical perovskite film as Fig. S3. Further it has to be assumed that all other phases present within the film show a featureless absorption around the $MAPbI_3$ band edge. All reflection spectra are fitted in an energy range close to the band edge of $MAPbI_3$, as explained below. The concentration c in the product $c*d$ is normalized, such that it reaches 100% at the end of the process or in its maximum. The fit of individual spectra only converges to physically meaningful values, when the absorption edge is significantly pronounced in the spectra. Therefore, this fitting yields reliable kinetic data only for $MAPbI_3$ concentrations larger than 20%.

The reflection spectra are fitted using

$$R(E) = R_0 + R_1\, exp(-2cd\, \alpha(E)\,) \qquad \text{(Eq SI 1)}$$

with the absorption coefficient α(E):

$$\alpha(E) = \alpha_0 \sqrt{E - E_g} \quad for\ E > E_g + E_u/2 \qquad \text{(Eq. SI 2)}$$

$$\alpha(E) = \alpha_0 \sqrt{E_u/2e}\ \ exp\big((E - E_g)/E_u\big) \quad for\ E < E_g + E_u/2 \qquad \text{(Eq. SI 3)}$$

where R_0 is the reflection from the surface assumed to be energy-independent, E_u is the Urbach energy of the band-tail and E_g is the band-gap of the material ($MAPbI_3$), c is the volume fraction of $MAPbI_3$, d the thickness of the film and α_0 the absorption constant of $MAPbI_3$ and R_1 is a proportionality factor. A fit with equation SI-1 to the reflectance spectrum obtained at the end of the synthesis process is depicted in Figure S4, showing very good agreement with the data. Fits are obtained for all reflection spectra in an energy range of 1.55 eV - 1.81 eV for the temperatures 80°C - 95 °C and 1.55 eV-1.97eV for 100°C. Note, that the analytical reflection fit describes the data very well with χ^2 below 0.001. However, the fit exhibits strong correlations between the fit variables. This means that a visually good fit can even be obtained with c fixed to c+-25%. In order to check the consistency of the applied fitting of reflection spectra, we compared its results to the evolution of the height of the absorption step during the synthesis, as shown in Figure S5.

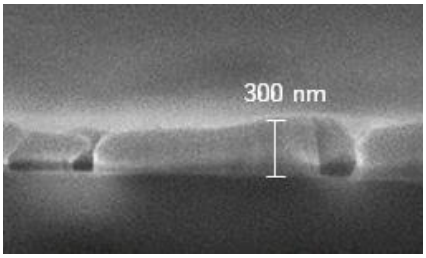

Fig. S3: SEM cross section image of a typical perovskite film

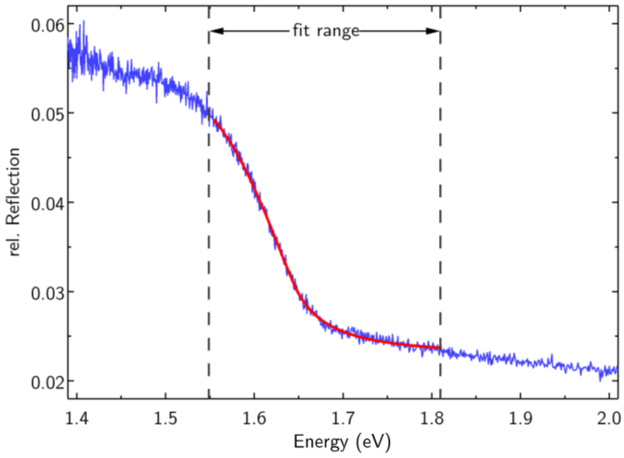

Fig. S4: Reflection spectrum of the final state of the process at 95 °C, together with a fit according to Eq.SI 1-3, exemplary.

Extraction of the absorption step: Spectra are taken as-measured and the edge-step is extracted by linear extrapolation of the regions above (R_1) and below (R_0) the absorption edge to an energy of 1.6 eV as shown in Fig. S5. The edge-step Γ is calculated by $\Gamma = \ln(R_1) - \ln(R_0)$. In some cases (in particular for the process at 85 °C) the as-measured reflection spectra from times before the formation of $MAPbI_3$ has started, show significant oscillations caused by internal reflection within the transparent precursor film, which disturb the extraction of the edge-step. To correct for this, the reflection spectra are normalized to an internal reference spectrum, taken during the annealing stage but well (4 minutes) before the beginning of the $MAPbI_3$ formation. The edge-step is then again extracted subsequently. The energy range used for the linear fits below and above the absorption edge are chosen such that the kinetic behavior of the edge-step reproduces that which was extracted by reflection model fitting. Ranges are shown in Table S1.

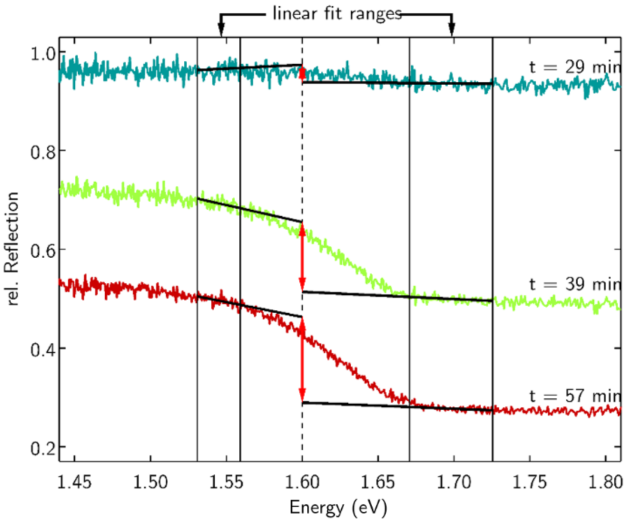

Fig. S5: Illustration of the extraction of the edge step from the individual reflectance spectra

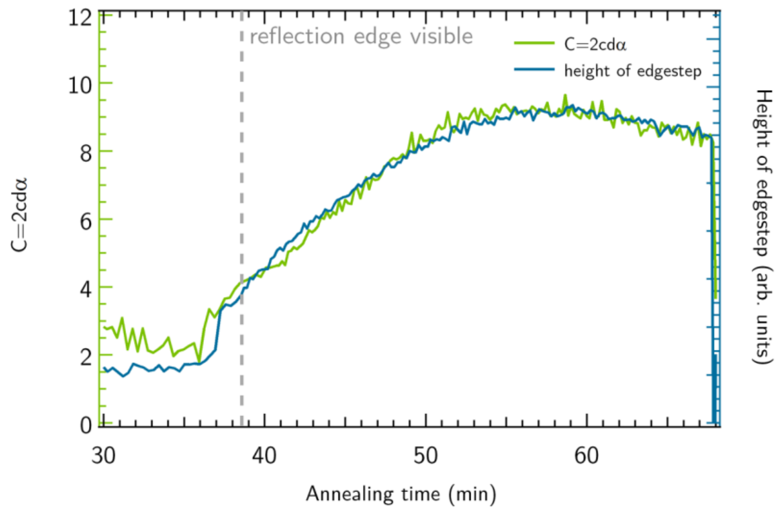

Fig. S6: Comparison of the concentration c as obtained from fitting the individual spectra and the edge step, obtained as described above.

Process temperature	Range high	Range low
100 °C	1.493 eV - 1.533 eV	1.684 eV - 1.738 eV
95 °C	1.530 eV - 1.561 eV	1.673 eV - 1.723 eV
90 °C	1.539 eV - 1.584 eV	1.644 eV - 1.742 eV
85 °C, 80°C	1.539 eV - 1.584 eV	1.657 eV - 1.690 eV

Table S1: Linear fitting ranges for extraction of the edge step in reflection spectra.

As shown in Fig. S6, the concentration value, ***c,*** as obtained from the fit of the absorption spectra agrees remarkably well with the absorption edge-step as described above. Hence we conclude that the herein used model describes the reflection sufficiently well and the obtained *c* can indeed be used as a relative measure of the concentration of $MAPbI_3$ within the film.

SI Note 3: Reproducibility

Photoluminescence is a very sensitive probe for any small changes in a material, as even minor changes may lead to changes in doping or defect concentration and thus alter the luminescence signal significantly. To ensure reproducibility the glovebox temperature was kept at 20°C, because it was noted that changes in the glovebox temperature led to changes in the kinetics of PL evolution as well as changes in the photoluminescence yield, as can be seen in Figure S7b. Furthermore, a graphite block was installed on the hotplate, in order to homogenize the surface temperature of the hotplate. The spatial homogeneity of the luminescence of the samples was controlled with an imaging camera. These measurements allowed for good reproducibility of the synthesis process as shown in Fig. S7 a.

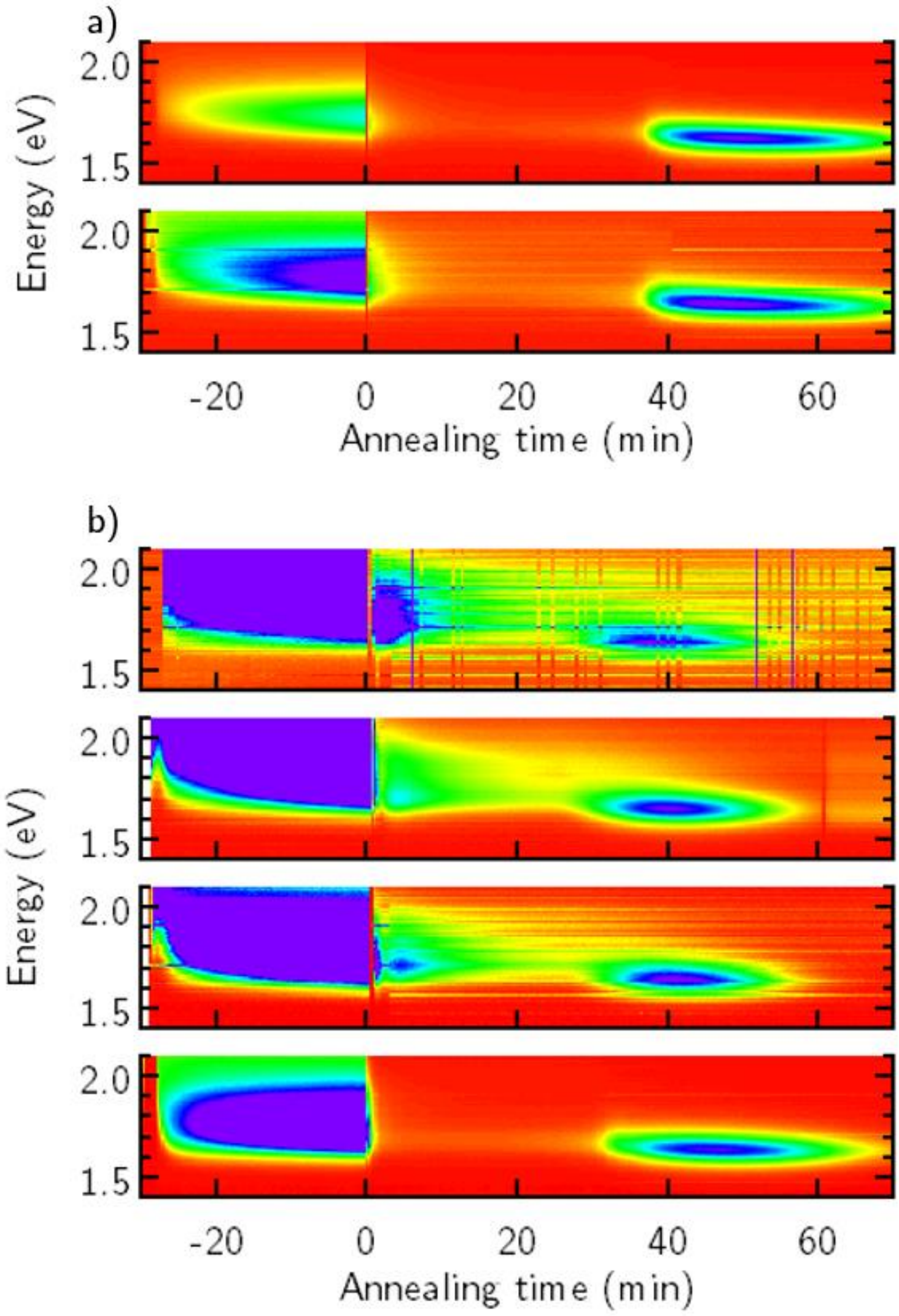

Fig. S7: Comparison of the evolution of the PL emission during drying and annealing for different $MAPbI_{3-x}Cl_x$ samples synthesized as described under methods and annealed at 100°C for 70 min. a) Shows the PL emission at constant 20°C Glovebox temperature. b) shows the PL emission at (uncontrolled varying) elevated glovebox temperatures between 30°C and 35°C .

For the ex-situ measurements, several samples were prepared from the same precursor solution and annealed at 100°C for varying annealing times. As shown in Figure S8, the photoluminescence intensity follows very similar kinetics for all samples.

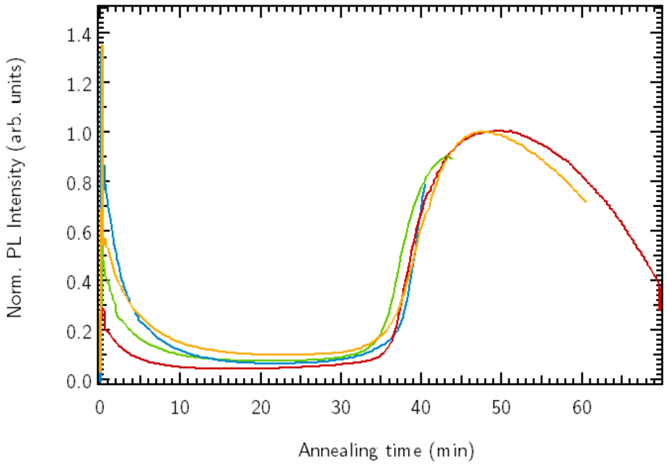

Fig. S8: Comparison of the evolution of the PL emission during annealing for different $MAPbI_{3-x}Cl_x$ samples synthesized as described under methods and annealed at 100°C for varying annealing times

The ex-situ measurements were performed directly after annealing in custom designed nitrogen filled chambers allowing for measurements without any exposure to ambient atmosphere. For this the sample was broken into several pieces allowing for parallel measurements. This way any effects of previous measurements on the sample or different times between annealing and measurement could be omitted. All measurements were concluded within 30 min after annealing. The sample was subsequently remeasured in the in-situ PL setup. No major changes in the PL emission energy or intensity could be observed.

The ex-situ measurements shown in this study were taken from two different synthesis runs, (indicated as green and red in Fig. S9). The synthesis procedure was kept the same for both runs. Fig.S9 indicates that the results from the two different synthesis runs follow similar trends further indicating that sufficient reproducibility was achieved.

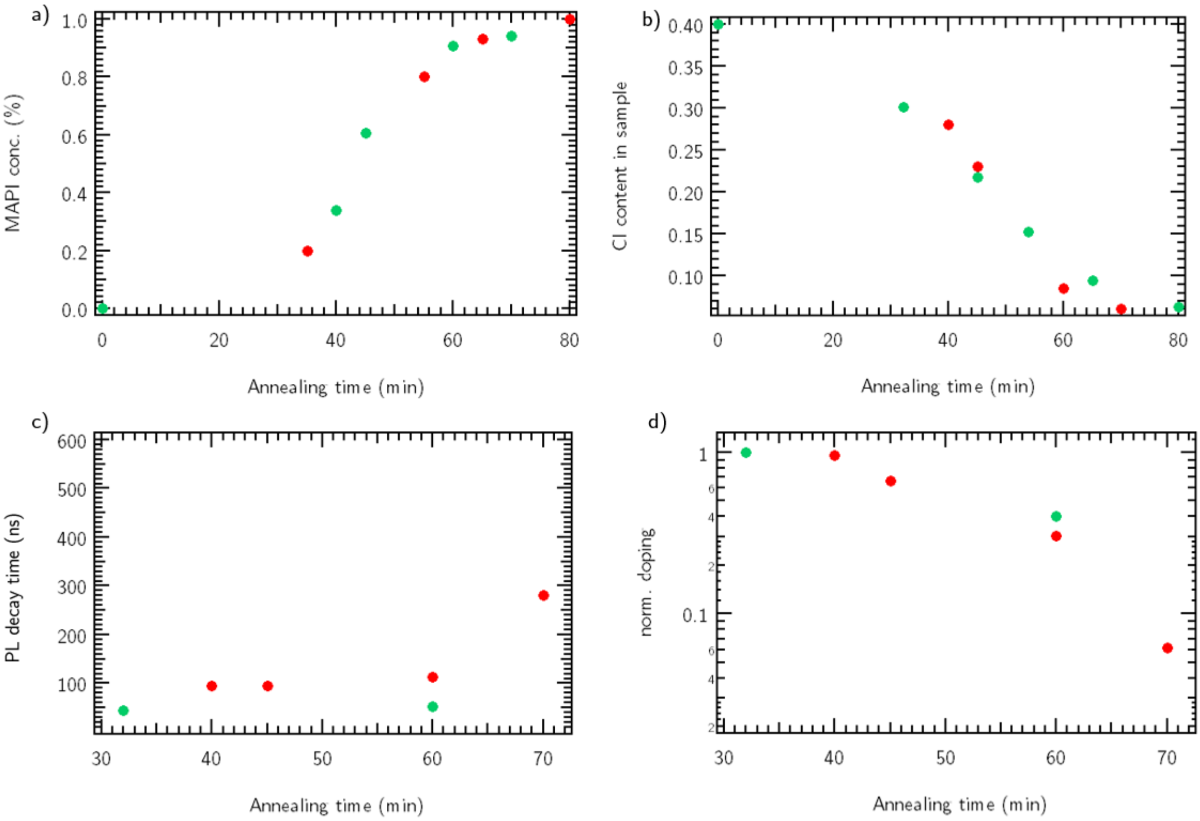

Fig. S9: Comparison of ex-situ measurements for different synthesis runs indicated by green and red. a) The concentration of $MAPbI_3$ as estimated from XRD for samples annealed for different times. b) The overall Cl content within the sample as measured with XRF. c) the PL decay time as measured with TRPL. d) the norm. doping as measured with TRPL

SI Note 4: In-situ monitoring of PbI_2/MAI derived synthesis

To allow a meaningful comparison of the $PbCl_2$ derived synthesis with a pure PbI_2 derived synthesis, the $PbCl_2$ recipe as described in the experimental section was followed as closely as possible. For this lead(II) iodide is used as purchased from Sigmar Aldrich instead of lead(II) chloride. All further synthesis steps are kept exactly as described in the methods section.

Figure S10 shows, that the concentration of $MAPI_3$ as obtained from the reflection analysis now begins to rise immediately after the placement of the sample on the hot plate. The photoluminescence yield and the peak energy show a very similar behavior as the mixed-halide sample, with a gradually decreasing PL peak energy and a maximum in the photoluminescence yield after a certain annealing time.

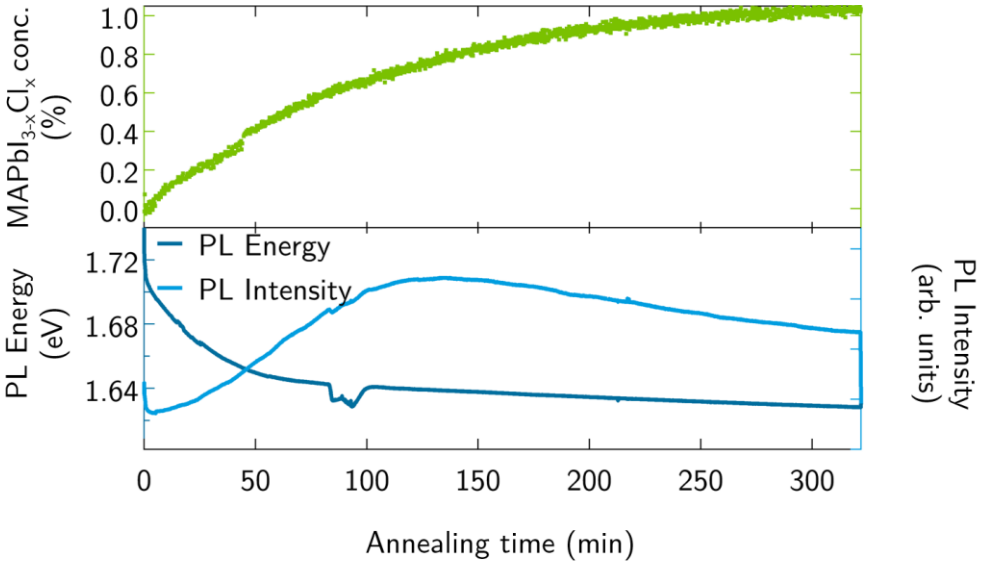

Fig. S10: Concentration of $MAPbI_3$ compared to the photoluminescence intensity and peak position as well as the process temperature for the PbI_2 derived synthesis.

SI Note 5: Calculation of the PLYQ and implied V_{oc}

The external PL quantum efficiency is calculated from the calibrated photon flux emitted from the sample, Φ_{PL}, exciting photon flux, Φ_{exc}, and absorption at the excitation wavelength $a(\lambda=455nm)$

$$PLQY = \frac{\phi_{PL}}{\phi_{exc}\, a(\lambda=455nm)} \qquad \text{(Eq. SI 4)}$$

For a large number of samples the ratio of the PL-yield at 100°C and the Pl-yield at room-temperature has been measured as shown in figure S11. It was found to be about a factor of 3 in average.

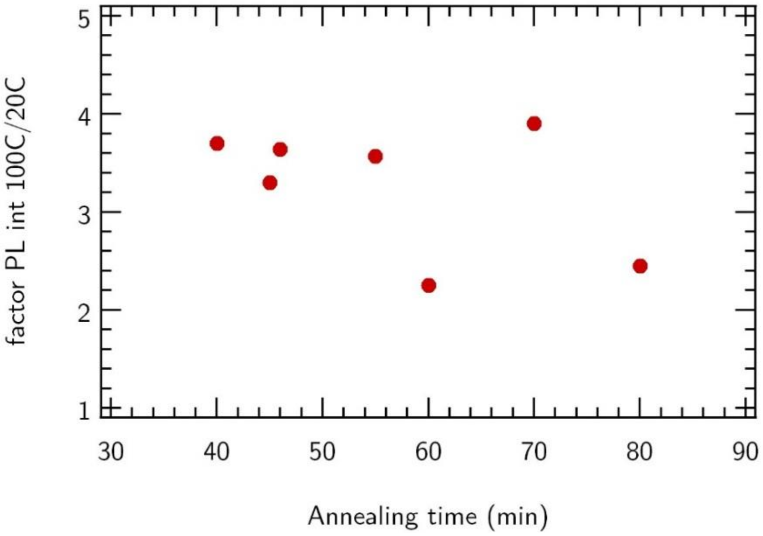

Fig. S11 The factor between the PL intensity at 100°C processing temperature and after subsequent cooling to RT is shown for samples annealed for different annealing times.

The quasi Fermi level splitting (or implied $V_{oc)}$ at room temperature is calculated by

$$\mu = \mu^{rad} + k_B T\, ln(PLQY/a_{780nm}\ \ ) \qquad \text{(Eq. SI 5)}$$

where μ^{rad} is the quasi-Fermi level splitting in the radiative limit, which in this study is approximated by the Shockley-Queisser-V_{oc} and the $PLQY$ here corresponds to the room temperature PL-quantum efficiency, which we estimated from the $PLQY'$ measured at 100°C by scaling with a factor of 3, which is the average factor between quantum efficiencies measured at 100°C and 20°C for a number of different samples, as shown in Figure S12. The absorptivity at 780nm is calculated from the reflection analysis according to equations SI1-SI3.

As shown in Figure S12, the absorption at 455nm does not change significantly during the annealing experiment.

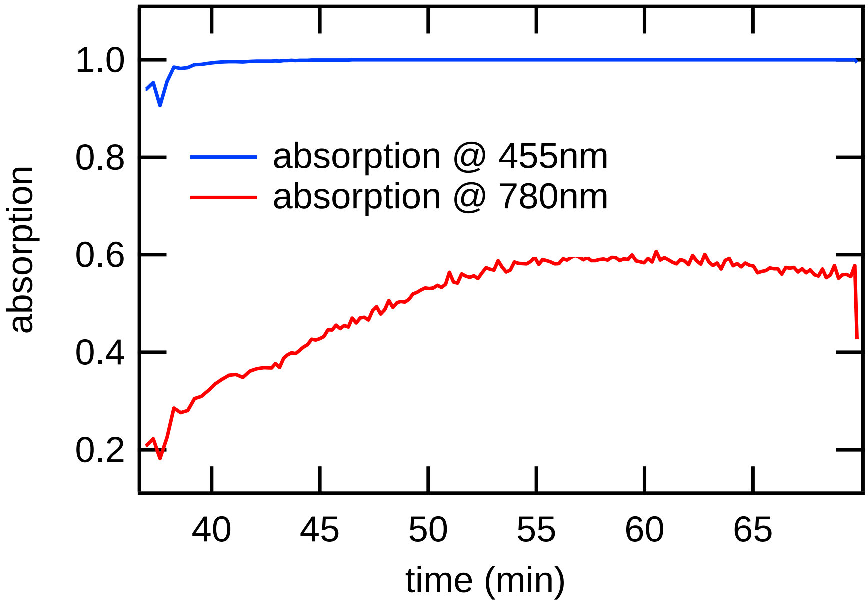

Fig. S12 Absorption of the perovskite film as a function of annealing time at 2 characteristic wavelengths

SI Note 6: Time-resolved photoluminescence

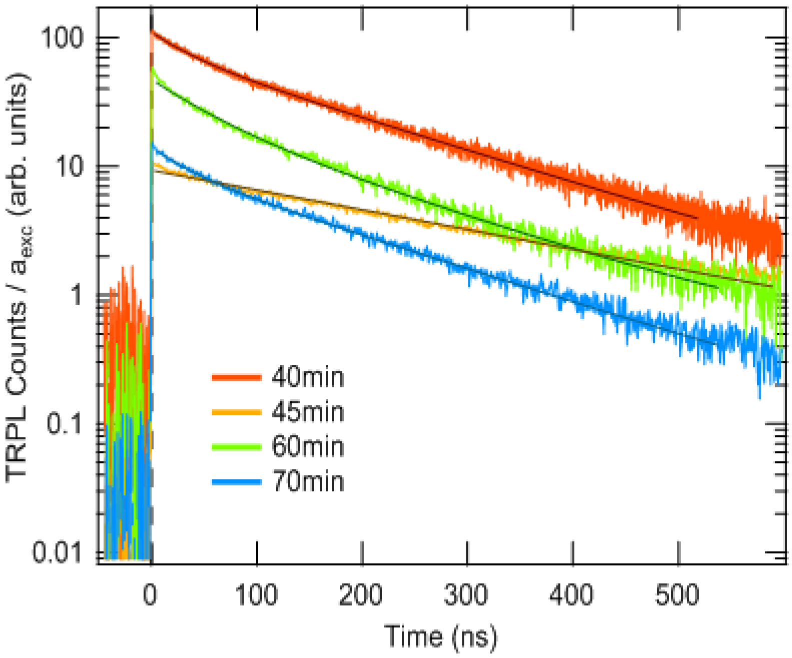

Fig. S13: Photoluminescence transients of $MAPbI_{3-x}Cl_x$ thin-film samples after respective times of annealing. Solid lines indicate a double exponential fit.

To ensure that the time-resolved measurement was performed in the low injection regime a series of different excitation intensities measured for each sample. From this an excitation density of $\Phi = 2.45\ 10^{15}$ photons/cm^3 per pulse was chosen to analyze the minority carrier lifetime of the samples. Figure S13 shows the transients recorded for samples from processes interrupted at the indicated annealing times. The recorded luminescence counts are normalized to the absorptivity at the laser wavelength of the breakoff samples. The transients were fitted with double exponentials and an effective lifetime was determined using

$\tau_{eff} = (a_1\tau_1 + a_2\tau_2)/(a_1 + a_2)$, except for the 70min transient where the double exponential was found to be overdetermined. In this case a single exponential was fitted.

Anneal (min)	a_1	σ_{a1}	τ_1 (ns)	$\sigma_{\tau1}$ (ns)	a_2	σ_{a2}	τ_2 (ns)	$\sigma_{\tau2}$ (ns)	τ_{eff} (ns)	$\sigma_{\tau eff}$ (ns)
40	34	12	36	18.4	76	5.8	170	6	129	31
45	21.5	8.5	50	14	25.7	7.81	157	18	108	25
60	4.4	2.03	32	12	10	1.28	163	17	128	39
70					9.3	1	282	12	282	12

Table S2: Results from fitting a double exponential to the time-resolved photoluminescence transients for break-off samples at several delay times. σ_{a1}, σ_{a2}, $\sigma_{\tau1}$, $\sigma_{\tau2}$,$\sigma_{\tau eff}$ are the standard deviations of the fitting parameters.

SI Note 7: Comparison of previously reported kinetics for Cl derived the formation of $MAPbI_3$

A comparison of the reported reaction kinetics at different temperatures (Fig. S14), shows that even though the "same" process was analyzed the kinetics observed in different setups do not agree. Chang et al., Unger et al. and Barrows et al. seem to see a delay in formation, while Moore et al. do not see a delay. However also the time of the delay varies significantly. Furthermore the reaction speed of the formation itself is very different. However it can be noted, that in case a delay is observed, the reaction kinetics after the delay agree very well, while when no delay is observed the perovskite formation occurs significantly slower.[4–7]

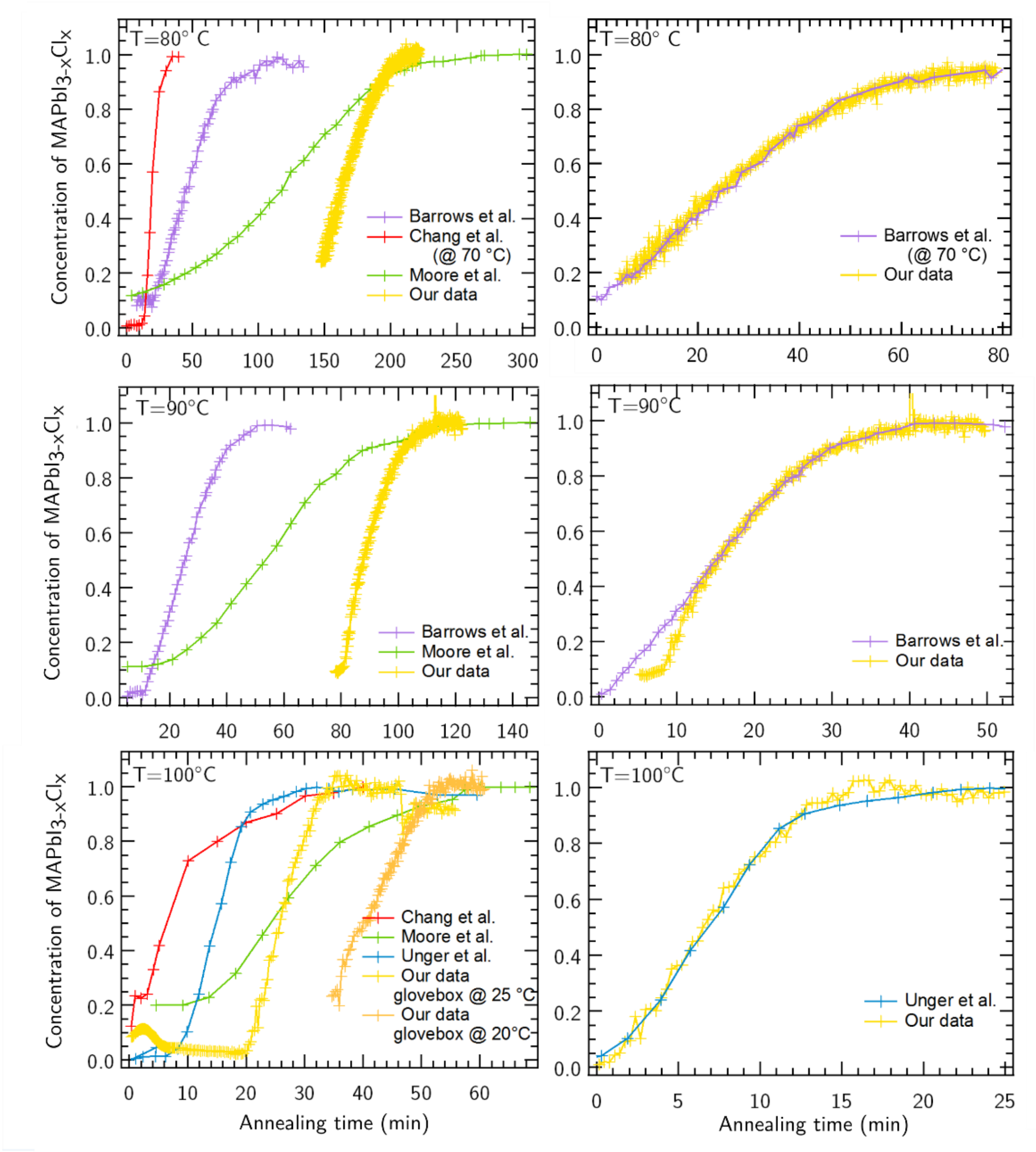

Fig. S14: Comparison of reported formation kinetics at different annealing temperatures. (80 °C, 90°C and 100°C)

	Measurement	**Environment**	**Substrate**	**Temperature characteristics**
Moore	GIWAXS	Air		
Barrows	GIWAXS	Air 40-45% r.H.	PEDOT:PSS	Temperature overshoot in first 10 min
Chang	GIWAXS	Air 40 % r.H.	Silicon	Substrate preheated
Unger	GIWAXS	Air	TiO_2 on Silicon	
Our data	Opt. reflection	N2	TiO_2 on FTO	

Table S3: Corresponding processing conditions to the reported formation kinetics of $PbCl_2$ derived $MAPbI_3$.

References:

(1) Baikie, T.; Barrow, N. S.; Fang, Y.; Keenan, P. J.; Slater, P. R.; Piltz, R. O.; Gutmann, M.; Mhaisalkar, S. G.; White, T. J. A Combined Single Crystal Neutron/X-Ray Diffraction and Solid-State Nuclear Magnetic Resonance Study of the Hybrid Perovskites CH3NH3PbX3 (X = I, Br and Cl). *J. Mater. Chem. A* **2015**, *3* (17), 9298–9307. https://doi.org/10.1039/C5TA01125F.

(2) Poglitsch, A.; Weber, D. Dynamic Disorder in Methylammoniumtrihalogenoplumbates (II) Observed by Millimeter-wave Spectroscopy. *The Journal of Chemical Physics* **1987**, *87* (11), 6373–6378. https://doi.org/10.1063/1.453467.

(3) P.Scherer. Bestimmung Der Größe Und Der Inneren Struktur von Kolloidteilchen. *Nachrichten von der Gesellschaft der Wissenschaften zu Göttingen, Mathematisch-Physikalische Klasse* **1918**, *1918* (Mathematica).

(4) Barrows, A. T.; Lilliu, S.; Pearson, A. J.; Babonneau, D.; Dunbar, A. D. F.; Lidzey, D. G. Monitoring the Formation of a CH3NH3PbI3–XClx Perovskite during Thermal Annealing Using X-Ray Scattering. *Advanced Functional Materials* **2016**, *26* (27), 4934–4942. https://doi.org/10.1002/adfm.201601309.

(5) Moore, D. T.; Sai, H.; Tan, K. W.; Smilgies, D.-M.; Zhang, W.; Snaith, H. J.; Wiesner, U.; Estroff, L. A. Crystallization Kinetics of Organic–Inorganic Trihalide Perovskites and the Role of the Lead Anion in Crystal Growth. *J. Am. Chem. Soc.* **2015**, *137* (6), 2350–2358. https://doi.org/10.1021/ja512117e.

(6) Unger, E. L.; Bowring, A. R.; Tassone, C. J.; Pool, V. L.; Gold-Parker, A.; Cheacharoen, R.; Stone, K. H.; Hoke, E. T.; Toney, M. F.; McGehee, M. D. Chloride in Lead Chloride-Derived Organo-Metal Halides for Perovskite-Absorber Solar Cells. *Chem. Mater.* **2014**, *26* (24), 7158–7165. https://doi.org/10.1021/cm503828b.

(7) Chang, C.-Y.; Huang, Y.-C.; Tsao, C.-S.; Su, W.-F. Formation Mechanism and Control of Perovskite Films from Solution to Crystalline Phase Studied by In-Situ Synchrotron Scattering. *ACS Appl. Mater. Interfaces* **2016**, *8* (40), 26712–26721. https://doi.org/10.1021/acsami.6b07468.